Available online at www.sciencedirect.com
ScienceDirect
International Journal of Heat and Mass Transfer 50 (2007) 3899–3912
International Journal of HEAT and MASS TRANSFER
www.elsevier.com/locate/ijhmt

Numerical solution of film condensation from turbulent flow of vapor–gas mixtures in vertical tubes

M.K. Groff, S.J. Ormiston *, H.M. Soliman

Department of Mechanical and Manufacturing Engineering, University of Manitoba, Winnipeg, Manitoba, Canada R3T 5V6

Received 17 August 2006; received in revised form 3 February 2007
Available online 16 April 2007

Abstract

A complete two-phase model is presented for film condensation from turbulent downward flow of vapor–gas mixtures in a vertical tube. The model solves the complete parabolic governing equations in both phases including a model for turbulence in each phase, with no need for additional correlation equations for interfacial heat and mass transfer. A finite volume method is used to form the discretized mean flow equations for conservation of mass, momentum, and energy. A fully coupled solution approach is used with a mesh that automatically adapts to the changing film thickness. The results of using three turbulence models involving combinations of mixing length and k–ε models in the film and mixture regions are compared. This new model is extensively compared with previous numerical and experimental studies. In the experimental comparisons, it was found that a model consisting of a k–ε turbulence model for both the film and the mixture flows produced the best agreement. Results are also presented for a parametric study of condensation from steam-air mixtures. The effects of changes to the inlet Reynolds number, the inlet gas mass fraction, and the inlet-to-wall temperature difference on the film thickness and heat transfer are presented and discussed. Local profiles of axial velocity, temperature, and gas mass fraction are also presented.

Keywords: Turbulent film condensation; Vertical tube; Non-condensable gas; Two-phase; Numerical model; Co-current flow

1. Introduction

The study of steam condensation in vertical tubes is important because of its relevance to the refrigeration, chemical processing, and thermal power generation industries. In the nuclear power generation industry, the effect of non-condensable gas during film condensation in a vertical tube is an important phenomenon in passive containment cooling systems. Since the pioneering analytical work of Nusselt [1], there have been numerous studies of external and internal condensation for various geometries. Studies of condensation in the presence of a non-condensable gas have shown the detrimental effect on heat transfer of the gas because of its build up at the liquid-mixture interface.

For the case of pure vapor condensation in vertical tubes, there have been simple correlations developed that yield the local heat transfer coefficient along the length of a tube [2,3], more advanced solutions developed from approximate sets of equations of motion [4–8], or more complete models [9,10]. For example, Panday [10] proposed a model for pure vapor condensation with turbulence in both the liquid film and the core. In this model, Panday solved a full set of parabolic governing equations including the conservation of mass, momentum, and energy in both the liquid film and the vapor core. Turbulence was modeled in both regions using a mixing length model developed by Pletcher [11].

For the case of condensation in the presence of a non-condensable gas, previous simplified theoretical analyses have employed either a heat and mass transfer analogy [12–15], stagnant film layer or diffusion-layer approaches [16,17], or self-similar velocity profile assumptions [18].

* Corresponding author. Tel.: +1 204 474 8639; fax: +1 204 275 7507.
E-mail address: sj_ormiston@umanitoba.ca (S.J. Ormiston).

0017-9310/$ - see front matter © 2007 Elsevier Ltd. All rights reserved.
doi:10.1016/j.ijheatmasstransfer.2007.02.012

Nomenclature

C_p	specific heat [J kg^{-1} K^{-1}]
$C_{\varepsilon 1}$	constant in the k–ε model
$C_{\varepsilon 2}$	constant in the k–ε model
C_μ	constant in the k–ε model
D	diffusion coefficient [m^2 s^{-1}]
D^*	damping function
f_2	constant in the k–ε model
f_μ	function in the k–ε model
g	gravitational acceleration [m s^{-2}]
h_{fg}	latent heat of vaporization [J kg^{-1}]
$h_{\mathrm{L},z}$	local interfacial heat transfer coefficient $(q''_z/(T_{\mathrm{int}} - T_{\mathrm{wall}}))$ [W m^{-2} K^{-1}]
h_z	local heat transfer coefficient $(q''_z/\Delta T_{\mathrm{in}})$ [W m^{-2} K^{-1}]
J	mass flow rate at control volume faces in the η direction [kg s^{-1}]
k	turbulent kinetic energy [m^2 s^{-2}]
ℓ	mixing length [m]
$\dot{m}$	total mass flow rate [kg s^{-1}]
Nu_z	local Nusselt number $(h_z 2r_0/\lambda_{\mathrm{L}})$
P	pressure [N m^{-2}]
P^+	dimensionless pressure gradient in mixing length model
Pr	Prandtl number $(\mu C_P/\lambda)$
q''_z	heat flux at the tube wall [W m^{-2}]
r	radial coordinate [m]
r_0	radius of tube [m]
$Re^{\mathrm{t}}_{\mathrm{L}}$	Reynolds number used in the k–ε model
Re_{in}	inlet Reynolds number $(\rho_{\mathrm{in}} u_{\mathrm{in}} 2r_0/\mu_{\mathrm{in}})$
Sc	Schmidt number $(\rho D/\mu)$
T	temperature [K]
ΔT_{in}	inlet-to-wall temperature difference $(T_{\mathrm{in}} - T_{\mathrm{wall}})$ [K]
T^*	dimensionless temperature $(T - T_{\mathrm{wall}})/(T_{\mathrm{in}} - T_{\mathrm{wall}})$
u	velocity in the z-direction [m s^{-1}]
u^*	dimensionless velocity in the z-direction (u/u_{in})
u_τ	friction velocity $(\sqrt{\tau/\rho})$ [m s^{-1}]
U^+	dimensionless axial velocity in the mixing length model
v	velocity in the r-direction [m s^{-1}]
V_0^+	dimensionless transverse velocity in the mixing length model
W	gas mass fraction
x	quality
y	transverse coordinate [m]
y^+	wall normal coordinate in the mixing length model
z	axial coordinate [m]
z^*	dimensionless axial coordinate $(z/2r_0)$

Greek symbols

γ	relative error
δ	thickness of condensate layer [m]
δ^*	dimensionless film thickness (δ/r_0)
δ_{BL}	boundary layer thickness in the mixing length model [m]
ε	dissipation rate [m^2 s^{-3}]
η	transformed coordinate in the r-direction
λ	thermal conductivity [W m^{-1} K^{-1}]
λ^{t}	turbulent thermal conductivity [W m^{-1} K^{-1}]
μ	dynamic viscosity [N s m^{-2}]
ρ	density [kg m^{-3}]
σ_k	constant in the k–ε model
σ_ε	constant in the k–ε model
τ	shear stress [N m^{-2}]
χ	transformed coordinate in the z-direction

Subscripts

b	bulk
cw	cooling water
eff	effective
ft	fully developed turbulent region
g	gas
in	tube inlet
int	liquid-mixture interface
L	liquid
M	vapor–gas mixture
0	wall or interface in mixing length model
sat	saturation condition
sb	bulk saturation
v	vapor
wall	tube wall

Superscripts

$''$	flux, per unit area
n	current iteration level
t	turbulent

Models using a more complete analysis solved the governing conservation equations in both the liquid film and the vapor–gas mixture and linked them with interfacial boundary conditions. Yuann [19] used such an approach to solve for turbulent film condensation from a steam-air mixture in vertical tubes. Yuann used a set of conservation equations similar to those in [10], except that turbulence was modeled using the low Reynolds number k–ε model of Jones and Launder [20] in both phases. Yuann also solved a gas conservation equation and used an empirical correlation to account for a wavy interface.

There have been several notable experiments performed to study condensation of both pure vapor and vapor–gas mixtures in vertical tubes. Goodykoontz and Dorsch [21] performed a series of experiments on pure steam condensation. More recent experiments included the presence of a

non-condensable gas [22,23]. Siddique [22] and Kuhn [23] both studied steam condensation in the presence of air or helium flowing downward in a vertical tube. Results from Siddique's experiments were presented for a wide range of inlet temperature, inlet gas mass fraction, and inlet Reynolds numbers. Kuhn presented a new, more accurate method in measuring the coolant bulk temperature along the tube.

The model presented in this work solves the complete two-dimensional, parabolic equations for film condensation from vapor–gas mixtures in vertical tubes. The governing equations are solved in the liquid phase and in the vapor–gas mixture phase, including a turbulence model in each phase. The solution method is based on an approach developed by Siow [24] for condensation in parallel-plate channels and applies only to co-current flows of a film and a gas–vapor mixture. The approach does not make use of a heat and mass transfer analogy, a diffusion layer, or a stagnant film analysis. Furthermore, no correlation equations are required to compute interfacial heat and mass transfer; these values are accounted for implicitly through boundary conditions applied at the liquid-mixture interface and are computed as part of the solution to the governing equations. In the numerical implementation, the present work uses a mesh that adapts automatically to the changing liquid film thickness along the tube and maintains a clearly defined interface between the phase regions. A fully coupled method is used to solve the discretized equations of conservation of mass, momentum, and energy in both phases simultaneously, producing excellent convergence behavior even for cases of high inlet gas mass fraction. The turbulence model equations are solved in a segregated manner. Three turbulence modeling approaches are compared: (1) Pletcher's mixing length model applied in both phases, (2) the Jones and Launder low Reynolds number k–ε model applied in both phases, and (3) a combination of the k–ε model applied in the core and the mixing length model applied in the film. The three approaches are evaluated by comparison of model predictions with experimental data from Goodykoontz and Dorsch [21], Siddique [22], and Kuhn [23]. This article presents the numerical model used, the comparisons of the three turbulence modeling approaches with experimental data, and a parametric study showing the effects of various independent parameters on condensation predictions made using the present model.

2. Mathematical model

2.1. Problem description

The problem being considered is shown schematically in Fig. 1. A downward turbulent flow of a mixture of a saturated vapor and a non-condensable gas enters a vertical tube of radius r_0 with a uniform temperature, T_{in}, a uniform axial velocity, u_{in}, a uniform pressure, P_{in}, and a uniform gas mass fraction, W_{in}. The temperature of the tube wall is maintained lower than that of the inlet mixture,

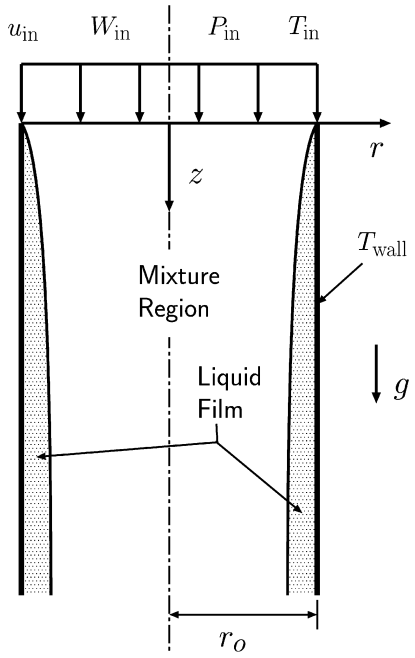

Fig. 1. Domain definition.

resulting in vapor condensation and a liquid film of thickness, δ, developing at the wall along the length of the tube. Starting from a film thickness of zero at the inlet, the liquid film flow is laminar near the inlet and can become turbulent at some distance down the tube. The flow is assumed to be axisymmetric due to the vertical orientation of the tube and the uniform inlet conditions.

2.2. Governing equations

In formulating the governing conservation equations it was assumed that the flow is steady and incompressible, the liquid-mixture interface is smooth, and the liquid and mixture are Newtonian fluids. The vapor–gas mixture was treated as an ideal-gas mixture and saturation conditions were assumed at the inlet and the liquid-mixture interface. The pressure, P, was assumed to be uniform in the radial direction (i.e., $dP/dr = 0$); however, P is allowed to vary in the axial (z) direction. Finally, the axial diffusion of heat, momentum, and mass are assumed to be negligible. Thermodynamic and transport properties of the fluids are calculated at the local conditions as described in [24].

The governing equations in cylindrical coordinates are as follows:

$$\frac{\partial}{\partial z}(\rho_L u_L) + \frac{1}{r}\frac{\partial}{\partial r}(r\rho_L v_L) = 0 \tag{1}$$

$$\frac{\partial}{\partial z}(\rho_L u_L u_L) + \frac{1}{r}\frac{\partial}{\partial r}(r\rho_L u_L v_L) = \frac{1}{r}\frac{\partial}{\partial r}\left(r\mu_{L,\text{eff}}\frac{\partial u_L}{\partial r}\right) + \rho_L g - \frac{dP}{dz} \tag{2}$$

$$\frac{\partial}{\partial z}(\rho_L u_L C_{P,L} T_L) + \frac{1}{r}\frac{\partial}{\partial r}(r\rho_L v_L C_{P,L} T_L) = \frac{1}{r}\frac{\partial}{\partial r}\left(r\lambda_{L,\text{eff}}\frac{\partial T_L}{\partial r}\right) \tag{3}$$

$$\frac{\partial}{\partial z}(\rho_M u_M) + \frac{1}{r}\frac{\partial}{\partial r}(r\rho_M v_M) = 0 \tag{4}$$

$$\frac{\partial}{\partial z}(\rho_M u_M u_M) + \frac{1}{r}\frac{\partial}{\partial r}(r\rho_M u_M v_M) = \frac{1}{r}\frac{\partial}{\partial r}\left(r\mu_{M,\mathrm{eff}}\frac{\partial u_M}{\partial r}\right) + \rho_M g - \frac{dP}{dz} \tag{5}$$

$$\frac{\partial}{\partial z}(\rho_M u_M C_{P,M} T_M) + \frac{1}{r}\frac{\partial}{\partial r}(r\rho_M v_M C_{P,M} T_M) = \frac{1}{r}\frac{\partial}{\partial r}\left(r\lambda_{M,\mathrm{eff}}\frac{\partial T_M}{\partial r}\right) + \frac{1}{r}\frac{\partial}{\partial r}\left(r\rho_M D_{\mathrm{eff}}(C_{P,g} - C_{P,v})\frac{\partial W}{\partial r}T_M\right) \tag{6}$$

$$\frac{\partial}{\partial z}(\rho_M u_M W) + \frac{1}{r}\frac{\partial}{\partial r}(r\rho_M v_M W) = \frac{1}{r}\frac{\partial}{\partial r}\left(r\rho_M D_{\mathrm{eff}}\frac{\partial W}{\partial r}\right) \tag{7}$$

Eqs. (1)–(3) govern the conservation of mass, momentum, and energy for the liquid film, while Eqs. (4)–(6) are the corresponding conservation equations for the gas phase (mixture) region. Eq. (7) ensures that the mass of gas is conserved. The effective viscosity and thermal conductivity in both phases are defined as follows:

$$\mu_{\mathrm{eff}} = \mu + \mu^t \tag{8}$$

$$\lambda_{\mathrm{eff}} = \lambda + \lambda^t \tag{9}$$

where

$$\lambda^t = \frac{\mu^t C_P}{Pr^t} \tag{10}$$

The effective diffusivity in the mixture region is defined as follows:

$$D_{\mathrm{eff}} = D + D^t \tag{11}$$

where

$$D^t = \frac{\mu_M^t}{\rho_M Sc_M^t} \tag{12}$$

In Eqs. (10) and (12), the turbulent Prandtl and Schmidt numbers are set equal to unity in both phases.

2.3. Turbulence models

The turbulent viscosity, μ^t, in each phase is determined by a choice of one of two modeling approaches: (1) Pletcher's mixing length model or (2) the Jones and Launder low Reynolds number k–ε model.

2.3.1. Pletcher's mixing length model

Pletcher [11] developed a mixing length model for turbulent boundary layer flow with transpiration that is based on the damping function proposed by van Driest. When using this model, the turbulent viscosity is determined with the following equation:

$$\mu^t = \rho\ell^2\left|\frac{\partial u}{\partial r}\right| \tag{13}$$

where ℓ is the mixing length defined by

$$\ell = 0.41D^* \quad \text{for } y \leqslant \frac{0.089\delta_{BL}}{0.41D^*} \tag{14}$$

and

$$\ell = 0.89\delta_{BL} \quad \text{for } y > \frac{0.089\delta_{BL}}{0.41D^*} \tag{15}$$

When this model is used in the liquid region, y is the distance measured from the wall. When it is used in the mixture region, y is the distance into the mixture, measured from the liquid-mixture interface. The boundary layer thickness, δ_{BL}, is defined as the location at which the velocity is 99% of the free-stream value. In the film, the free-stream value is the velocity at the liquid-mixture interface. In the mixture a velocity relative to the interface velocity is used and the free-stream value is the center line velocity. The damping function, D^*, is given by

$$D^* = 1 - \exp\left[\frac{-\rho_0 y}{26\mu_0}\left(\frac{\tau\tau_{ft}}{\rho_0\tau_0}\right)^{1/2}\right] \tag{16}$$

The subscript 0 in the above equation refers to the wall for the liquid region and the interface for the mixture region. The shear stress τ is defined by

$$\tau = \tau_0(1 + V_0^+ U^+ + P^+ y^+) \tag{17}$$

where

$$V_0^+ = \frac{v_0}{u_\tau}, \quad U^+ = \frac{u}{u_\tau}, \quad P^+ = \left(\frac{\mu}{\rho^2 u_\tau^3}\right)\frac{dP}{dz}, \quad y^+ = \frac{\rho y u_\tau}{\mu}, \quad u_\tau = \sqrt{\tau_0/\rho_0} \tag{18}$$

The shear stress for a fully developed turbulent region, τ_{ft}, is evaluated at $y^+ = 26$.

2.3.2. The Jones and Launder k–ε model

In the Jones and Launder low Reynolds number k–ε model [20], the turbulent viscosity is determined from the solution of the transport equations for the turbulent kinetic energy and the dissipation rate. One of the benefits of this model is that it is valid in the viscous sub-layer and therefore it can be applied right up to the wall in the liquid region and to the interface in the mixture region.

The turbulent kinetic energy and dissipation transport equations have the same form in both the liquid film and the mixture region, and will therefore be shown only once for the liquid region. The transport equations are

$$\frac{\partial}{\partial z}(\rho_L u_L k_L) + \frac{1}{r}\frac{\partial}{\partial r}(r\rho_L v_L k_L) = \frac{1}{r}\frac{\partial}{\partial r}\left[r\left(\mu_L + \frac{\mu_L^t}{\sigma_k}\right)\frac{\partial k_L}{\partial r}\right] + \mu_L^t\left(\frac{\partial u_L}{\partial r}\right)^2 - \rho_L\varepsilon_L - 2\mu_L\left(\frac{\partial\sqrt{k_L}}{\partial r}\right)^2 \tag{19}$$

and

$$\frac{\partial}{\partial z}(\rho_L u_L \varepsilon_L) + \frac{1}{r}\frac{\partial}{\partial r}(r\rho_L v_L \varepsilon_L) = \frac{1}{r}\frac{\partial}{\partial r}\left[r\left(\mu_L + \frac{\mu_L^t}{\sigma_\varepsilon}\right)\frac{\partial \varepsilon_L}{\partial r}\right] + C_{\varepsilon 1}\frac{\varepsilon_L}{k_L}\mu_L^t\left(\frac{\partial u_L}{\partial r}\right)^2 - C_{\varepsilon 2} f_2 \rho_L \frac{\varepsilon_L^2}{k_L} + 2\frac{\mu_L \mu_L^t}{\rho_L}\left(\frac{\partial^2 u_L}{\partial r^2}\right)^2 \quad (20)$$

The constants used in Eqs. (19) and (20) are: $\sigma_k = 1.0$; $\sigma_\varepsilon = 1.3$; $C_{\varepsilon 1} = 1.55$; $f_2 = 1$; and

$$C_{\varepsilon 2} = 2.0(1 - 0.3\exp(-Re_L^{t^2})) \quad (21)$$

where $Re_L^t = \frac{\rho_L k_L^2}{\mu_L \varepsilon_L}$. The turbulent viscosity is determined from

$$\mu_L^t = (C_\mu f_\mu \rho_L k_L^2)/\varepsilon_L \quad (22)$$

where $C_\mu = 0.09$ and

$$f_\mu = \exp(-2.5/(1 + Re_L^t/50)) \quad (23)$$

2.3.3. Definitions of the three overall turbulence models

Three overall turbulence models were defined in terms of the choice of model in each phase:

- TM1: the Pletcher mixing length model in both phases.
- TM2: the Jones and Launder low Reynolds number k–ε model in both phases.
- TM3: the Pletcher mixing length model in the liquid film and the Jones and Launder low Reynolds number k–ε model in the mixture region.

These definitions will be used later in the presentation of model results.

2.4. Boundary conditions

The boundary conditions for Eqs. (1)–(7), (19) and (20) are

- At the tube wall ($r = r_0$):

$$u_L = v_L = k_L = \varepsilon_L = 0 \quad (24)$$

$$T_L = T_{wall} \quad (25)$$

- At the liquid-mixture interface ($r = r_0 - \delta$):

$$u_L = u_M \quad (26)$$

$$T_L = T_M = T_{sat} \quad (27)$$

$$\mu_{L,eff}\frac{\partial u_L}{\partial r} = \mu_{M,eff}\frac{\partial u_M}{\partial r} \quad (28)$$

$$\left(\rho_L v_L + \rho_L u_L \frac{d\delta}{dz}\right)_{int} = \left(\rho_M v_M + \rho_M u_M \frac{d\delta}{dz}\right)_{int} = J''_{int} \quad (29)$$

$$\lambda_{L,eff}\frac{\partial T_L}{\partial r} = \lambda_{M,eff}\frac{\partial T_M}{\partial r} - J''_{int} h_{fg} \quad (30)$$

$$J''_{int} W - \rho_M D_{eff}\frac{\partial W}{\partial r} = 0 \quad (31)$$

$$k_L = \varepsilon_L = 0 \quad (32)$$

- At the center line ($r = 0$):

$$\frac{\partial u_M}{\partial r} = \frac{\partial T_M}{\partial r} = \frac{\partial W}{\partial r} = \frac{\partial k_M}{\partial r} = \frac{\partial \varepsilon_M}{\partial r} = 0 \quad (33)$$

$$v_M = 0 \quad (34)$$

At the inlet, the film thickness is zero, the liquid temperature is set to T_{wall}, and the velocities in the liquid region are set to zero. In the mixture region, uniform inlet profiles of u, T, W, and P are specified; the v velocity is set to zero. When the k–ε model is used, k and ε inlet values are equal to zero in the liquid region. In the mixture region, a uniform k inlet profile is specified, computed using $k_M = 1.5I^2 u_{in}^2$, where I is the turbulence intensity; $I = 0.037$ was used in this work. A uniform inlet profile for ε_M was computed using $\varepsilon_M = k_M^{3/2}/(0.6r_0)$.

One additional equation is required to complete the mathematical model. The local pressure gradient, dP/dz, is determined using the following global mass conservation constraint:

$$\int_0^{r_0-\delta} \rho_M u_M r\,dr + \int_{r_0-\delta}^{r_0} \rho_L u_L r\,dr = \frac{\dot{m}_{in}}{2\pi} \quad (35)$$

For a specified vapor–gas mixture at the inlet of the tube, the required input values for solving the above model are the radius r_0, u_{in} (or Re_{in}), T_{in} (or P_{in}), W_{in}, and T_{wall} (or ΔT_{in}).

3. Numerical solution method

A numerical solution was developed based on the mathematical model described by Eqs. (1)–(7) plus boundary equations and auxiliary relations. Before discretizing the transport equations and boundary conditions, a transformation of coordinates was made from the r–z coordinate system to an η–χ coordinate system, such that the center line is at $\eta = 0$, the liquid-mixture interface is at $\eta = 1$, and the wall is at $\eta = 2$. The equations that relate the η–χ coordinate system to the r–z coordinate system are [25]

$$\chi = z \quad \text{for } z \geqslant 0 \quad (36)$$

$$\eta = 2 - \frac{(r_0 - r)}{\delta} \quad \text{for } (r_0 - \delta) \leqslant r \leqslant r_0 \quad (37)$$

and

$$\eta = \frac{r}{(r_0 - \delta)} \quad \text{for } 0 \leqslant r \leqslant (r_0 - \delta) \quad (38)$$

The solution domain was divided into control volumes and the transformed equations were discretized using a finite volume method [25]. For convenience, the v-velocity component was substituted with the mass flux J'', which is defined in Eq. (29). Throughout the discretization process, upwind approximations were used for the control volume faces in the χ-direction and the exponential differencing scheme was used for the control volume faces in the η-direction. A Newton–Raphson linearization was used on all

non-linear terms in Eqs. (1)–(7). A set of non-linear algebraic equations was produced for the eleven solution fields ($u_L, J''_L, T_L, u_M, J''_M, T_M, W, k_M, k_L, \varepsilon_M$, and ε_L) and the two scalars ($dP/d\chi$ and δ). The kinetic energy and dissipation rate equations were solved only as needed. Zero-width control volumes were used to apply boundary conditions at the center line, the liquid-mixture interface, and the wall.

The discretized equations were solved starting at station 1 (the first row of control volumes in the liquid and the mixture) and proceeding station-by-station in the χ-direction. The coupled linearized equation set (excluding the turbulence model equations) was solved directly using a bordered-matrix algorithm and a block TDMA [25]. After each solution of the linearized equations, under-relaxation was applied to the u_L, J''_L, u_M, and J''_M fields and to the values of $dP/d\chi$, and δ. Typical values of the relaxation factors used are: 0.6 for u and J'', and 0.1 and 0.2 for $dP/d\chi$, and δ, respectively. The turbulence model equations were solved either by simple algebra when the mixing length model was employed, or by a TDMA for each equation when the k–ε model was used. To achieve convergence of the full set of coupled, non-linear equations at an axial station, iteration of the block TDMA and the turbulence model equation solution was performed. Overall convergence of the fields from the coupled equation solution was evaluated using

$$\gamma = \left| \frac{\varphi^n - \varphi^{n-1}}{\varphi^n} \right| \tag{39}$$

where $\varphi = \left\{ u, J'', T, W, \delta, \frac{dP}{d\chi} \right\}$. Convergence was declared when $\gamma < 1 \times 10^{-7}$ for all nodal values of all the fields was achieved. When the k–ε model was used, convergence of both the fields was evaluated using

$$\gamma = \left| \frac{\varphi^n - \varphi^{n-1}}{\varphi^n_{max} - \varphi^n_{min}} \right| \tag{40}$$

Convergence was declared when $\gamma < 1 \times 10^{-7}$ for all the nodal values of k and ε was achieved. When the mixing length model was used, convergence of all nodal values of the turbulent viscosity was checked using Eq. (40), and convergence was declared when $\gamma < 1 \times 10^{-5}$ was achieved. The station-by-station marching solution proceeded along the tube until the prescribed tube length was reached, complete condensation was achieved, or flow reversal (negative values of u) occurred.

In order to ensure grid-independent results, tests were performed using grids with nodal distributions of 40–100 nodes in the liquid region, 60–120 nodes in the mixture region, and 2000–5000 nodes in the axial direction for a tube length of 2.2 m. In the radial direction, the grid was uniformly distributed in η in the liquid region and geometrically contracted toward the interface in the mixture region. In the axial direction, the grid spacing expanded geometrically away from the inlet at the same rate in both phase regions. In these tests, the relative change between results for grids of different resolutions were computed for values of selected u and T profiles and for the axial distributions of δ, $dP/d\chi$, and local Nusselt number. A grid of 80 nodes in the liquid region and 100 nodes in the mixture region at each station and 4000 nodes in the axial direction produced changes of less than 0.1% relative to more refined grids. This level of grid resolution or better was used for all results presented here.

The numerical solution was implemented in an in-house computer code which was thoroughly tested for consistency. In addition, both laminar and turbulent flow validation tests were performed as checks of the mathematical model. For the case of laminar flow, good agreement was obtained when the results from the model were compared with the analytical solution of Nusselt [1], with the numerical results of Dobran and Thorsen [4], and with an analytical solution for end of condensation conditions [25]. For the case of turbulent flow, the code was set up to model turbulent single phase flow in a pipe, and the Jones and Launder low Reynolds number k–ε model was used. The model results were then compared with the experimental data of Nikuradse [26] and good agreement was obtained [25].

4. Comparison with previous studies

4.1. Numerical studies

The results of the present model were compared with those from two previous numerical studies mentioned earlier: Panday [10] and Yuann [19]. For the first comparison, the present model used the Pletcher mixing length model in both phases (model TM1) for condensation of pure steam to match the approach of Panday. Fig. 2 is a plot of the axial variation of local Nusselt number for two inlet Reynolds numbers. Also shown in the plot is the prediction of the correlation by Chen et al. [3], which was used for comparison in [10]. Fig. 2a shows that both numerical results and the correlation are in good agreement at a Reynolds number of 37,700. In Fig. 2b, the results at a Reynolds number of 94,300 show that there is greater deviation between the two numerical results, with the present model having better agreement with the correlation of Chen et al.

Fig. 3a and b shows comparisons of the present model and the results of Yuann [19] for axial variations of dimensionless film thickness and local interfacial heat transfer coefficient. These comparisons are made for pure steam and for a steam-air mixture with an inlet mass fraction of 0.4. In this comparison, the present model used the low Reynolds number k–ε model of Jones and Launder to model turbulence in both phases (model TM2) to be consistent with Yuann's approach. Note that the local interfacial heat transfer coefficient plotted in Fig. 3b is defined as $q''_z/(T_{int} - T_{wall})$ to be consistent with the definition used by Yuann. The results of the two numerical models shown in Fig. 3 are more similar for the case with pure steam than for the case with an inlet gas mass fraction of 40%. Although the governing equations and the turbulence model are similar between the two models, there are several

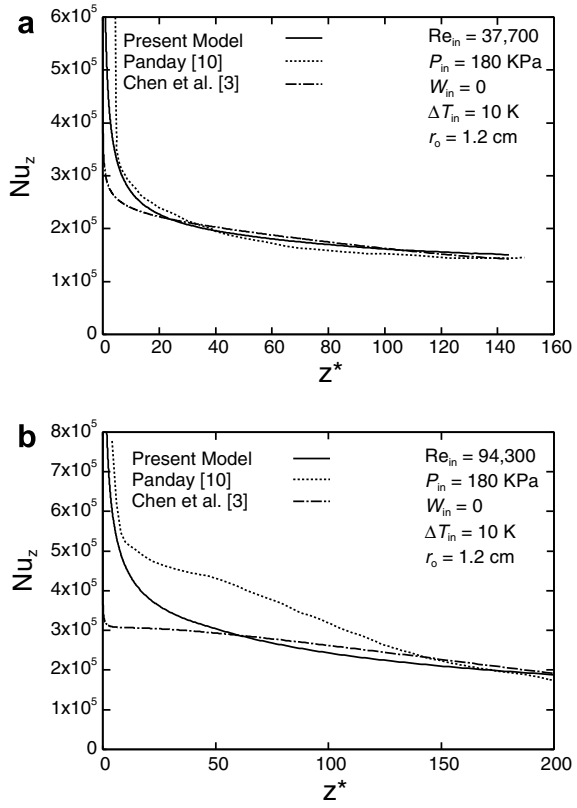

Fig. 2. Local Nusselt number comparison with Panday [10] and Chen et al. [3] for (a) $Re_{in} = 37{,}700$ and (b) $Re_{in} = 94{,}300$.

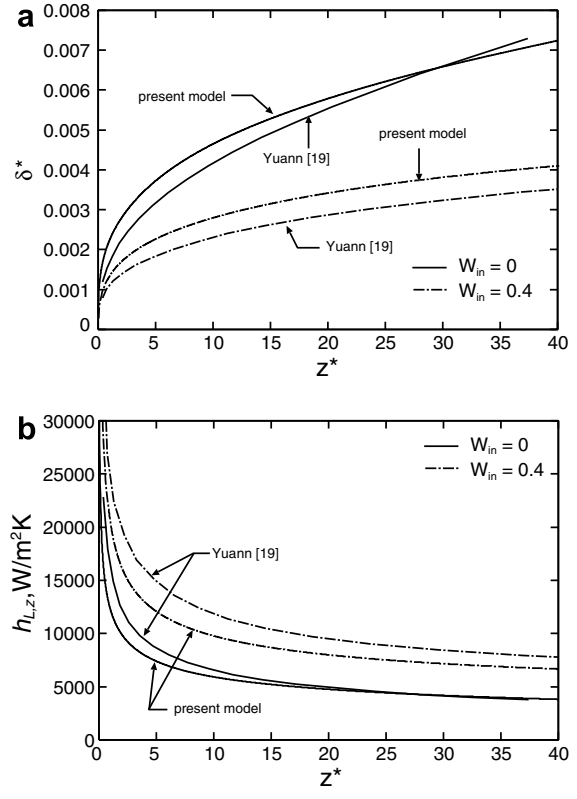

Fig. 3. Comparison with Yuann [19] for $P_{in} = 276$ kPa, $\dot{m}_{in} = 40$ kg/h, with $\Delta T_{in} = 7.53$ K for $W_{in} = 0$ and $\Delta T_{in} = 2.13$ K for $W_{in} = 0.4$; (a) dimensionless film thickness, and (b) local heat transfer coefficient.

differences that could explain the deviation in the results. First, Yuann used a boundary condition of $\frac{\partial v}{\partial r} = 0$ at the center line. Second, when the inlet mass flow rate, temperature, and pressure were set to match Yuann's data for a given tube, it was found that the resulting inlet Reynolds number did not always agree. Moreover, the agreement was good for pure steam, but for air-steam mixtures the inlet Reynolds number given by Yuann was always higher than those computed for the present model, with the deviation increasing with W_{in}. Because the equations for calculation of the mixture properties were the same for Yuann and the present model, it was concluded that the evaluation of air viscosity by Yuann was the source of the discrepancy. The values of air viscosity in the present model were verified against standard tables. Finally, Yuann used a grid structure in the r–z co-ordinate system. This grid structure requires a complicated method of advancing from one station to the next. The present model, on the other hand, always has the liquid-mixture interface clearly defined with the same number of radial-direction nodes at all stations along the tube. Further details on these comparisons can be found in [25].

4.2. Experimental studies

The experiments of Goodykoontz and Dorsch [21], Siddique [22], and Kuhn [23] were selected for assessment of the present numerical model predictions using the three

Table 1
Experimental runs chosen

Run #	Re_{in}	P_{in} [kPa]	ΔT_{in} [K]	x_{in}
Runs chosen from Goodykoontz and Dorsch [21]				
3	82,900	243	11.8	0.99
4	90,500	252	12.6	0.99
5	37,600	269	14.8	0.96
6	45,100	307	13.2	0.96
7	64,500	265	16.8	0.97
9	27,800	138	12.5	0.94
				W_{in}
Runs chosen from Siddique [22]				
1	6,000	107	7.4	0.09
6	7,330	133	28.8	0.33
13	4,840	389	26.2	0.11
17	5,790	475	60.3	0.34
35	17,300	109	0.7	0.11
40	23,700	137	1.8	0.35
47	19,200	386	6.5	0.10
52	23,100	485	15.3	0.35
Runs chosen from Kuhn [23]				
1.1–1	36,500	116	4.3	0
1.1–5	32,200	502	17.8	0
1.4–2	18,500	108	5.9	0
1.4–5	15,700	499	12.9	0
3.5–2	48,900	205	13.9	0.38
3.5–5	43,700	493	28.8	0.37
4.5–2	24,500	202	20.7	0.40
4.5–5	23,400	503	36.2	0.38

turbulence models defined in Section 2.3. Test cases covering a variety of conditions were chosen from each of these three experiments, and for each case the program was run using turbulence models TM1, TM2, and TM3. In all cases, the model inlet boundary conditions were prescribed with fully developed single phase turbulent flow profiles. These profiles were obtained from the exit plane of a separate code run for a sufficiently long tube under the same operating conditions. In addition, the tube wall temperature was prescribed using a polynomial curve fit to the wall temperature data given in the experimental results.

Goodykoontz and Dorsch [21] presented results for 14 experiments on condensation of pure steam in a vertical tube with $r_0 = 7.95$ mm. The six runs from Goodykoontz and Dorsch's experiments that were chosen for comparison are summarized in Table 1. Because the inlet quality in the present model is always 100% and that in the Goodykoontz and Dorsch experiments was not, the comparison of results is based on an adjustment of the z-axis origin for the numerical results. An inlet boundary condition of 100% quality was used in the present numerical model, and for comparison purposes, $z = 0$ was re-defined as the point where the code-predicted quality was equal to the inlet quality given in Table 1. Fig. 4a–c are plots comparing the local heat transfer coefficient from the present numerical model using turbulence models TM1, TM2, and TM3,

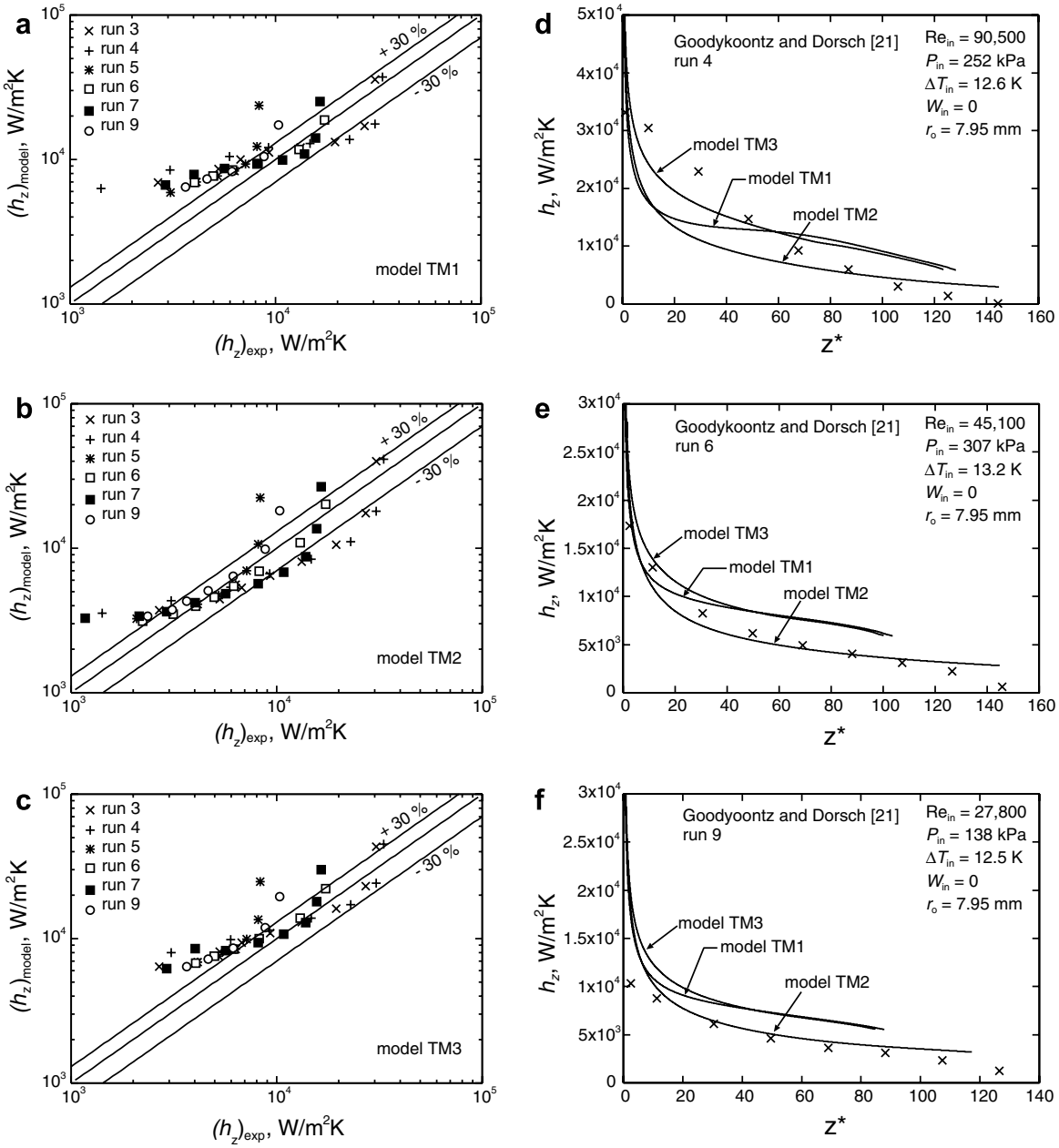

Fig. 4. Comparisons with Goodykoontz and Dorsch [21] of overall heat transfer coefficient for six runs using (a) model TM1, (b) model TM2, and (c) model TM3, and of local heat transfer coefficient using all three models for (d) run 4, (e) run 6, and (f) run 9.

respectively, with the experimental results. Overall, model comparisons show reasonable agreement with the experiment over this wide range of conditions. Model TM2, however, produced the best agreement, with 61% of the numerical data being within ±40% of the experimental data. Sample results of comparisons of the numerical and experimental results for axial variation of local heat transfer coefficient are shown in Fig. 4d–f. The model TM2 predictions show a reasonably good agreement with the experiments, especially for runs 6 and 9. Models TM1 and TM3 tend to significantly over-predict the heat transfer coefficient in the last two-thirds of the tube length.

Siddique [22] presented a total of 52 steam-air experimental runs in a tube with $r_0 = 2.30$ cm, and the eight which were chosen for comparison are listed in Table 1. In Fig. 5, the local heat transfer coefficient calculated from the numerical model using each of the three turbulence models is plotted versus Siddique's experimental results for those eight runs. Fig. 5a shows that there is significant deviation from the experiment in the results for model TM1. The results for models TM2 and TM3 are plotted in Fig. 5b and c, respectively. The results from using models TM2 and TM3 are very similar to each other, with the results for model TM3 being marginally better. For these eight runs, the predictions using model TM3 were within ±30% of the experimental results for 64% of the data and within ±40% of the experimental results for 89% of the data. The axial distributions of the local heat transfer

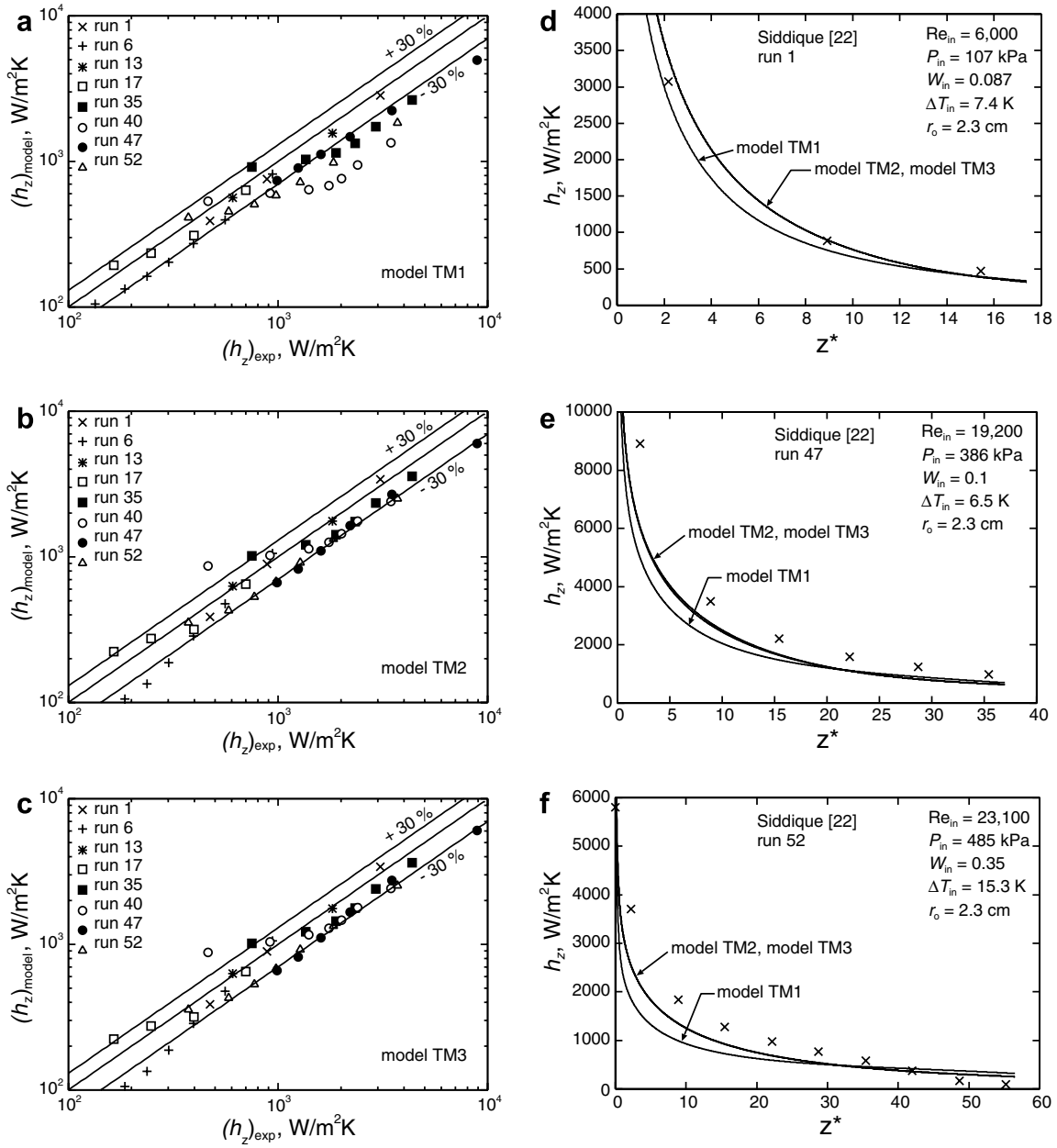

Fig. 5. Comparison with Siddique [22] of overall heat transfer coefficient for eight runs using (a) model TM1, (b) model TM2, and (c) model TM3, and of local heat transfer coefficient using all three models for (a) run 1, (b) run 47, and (c) run 52.

coefficient for three of the eight test cases are plotted in Fig. 5d–f. These plots show that the results using models TM2 and TM3 are very similar and are both better than those produced using model TM1.

Kuhn [23] presented a total of 81 experimental runs involving steam (with and without air) for a tube with $r_0 = 2.375$ cm. From this set of runs, four runs with pure steam and four runs with high inlet gas mass fraction were selected, as summarized in Table 1. Fig. 6 shows the comparison with experimental data of the present numerical results using the three turbulence models. Fig. 6a shows greater deviation exists between the model TM1 results and the experimental data for the runs containing air than for the runs with pure steam. The agreement with the experiments improves for model TM3 results, seen in Fig. 6c, but is best for model TM2, as seen in Fig. 6b. For these eight runs, the model TM2 results were within ±15% of the experimental results for 86% of the data and within ±30% of the experimental results for 98% of the data. The good agreement between model TM2 predictions and the experimental results of Kuhn can also be seen in the axial distributions of local heat transfer coefficient plotted for three runs in Fig. 6d–f.

It is pertinent to briefly discuss the different methods of evaluating the coolant bulk temperature that were used in each of the three experiments that were chosen for compar-

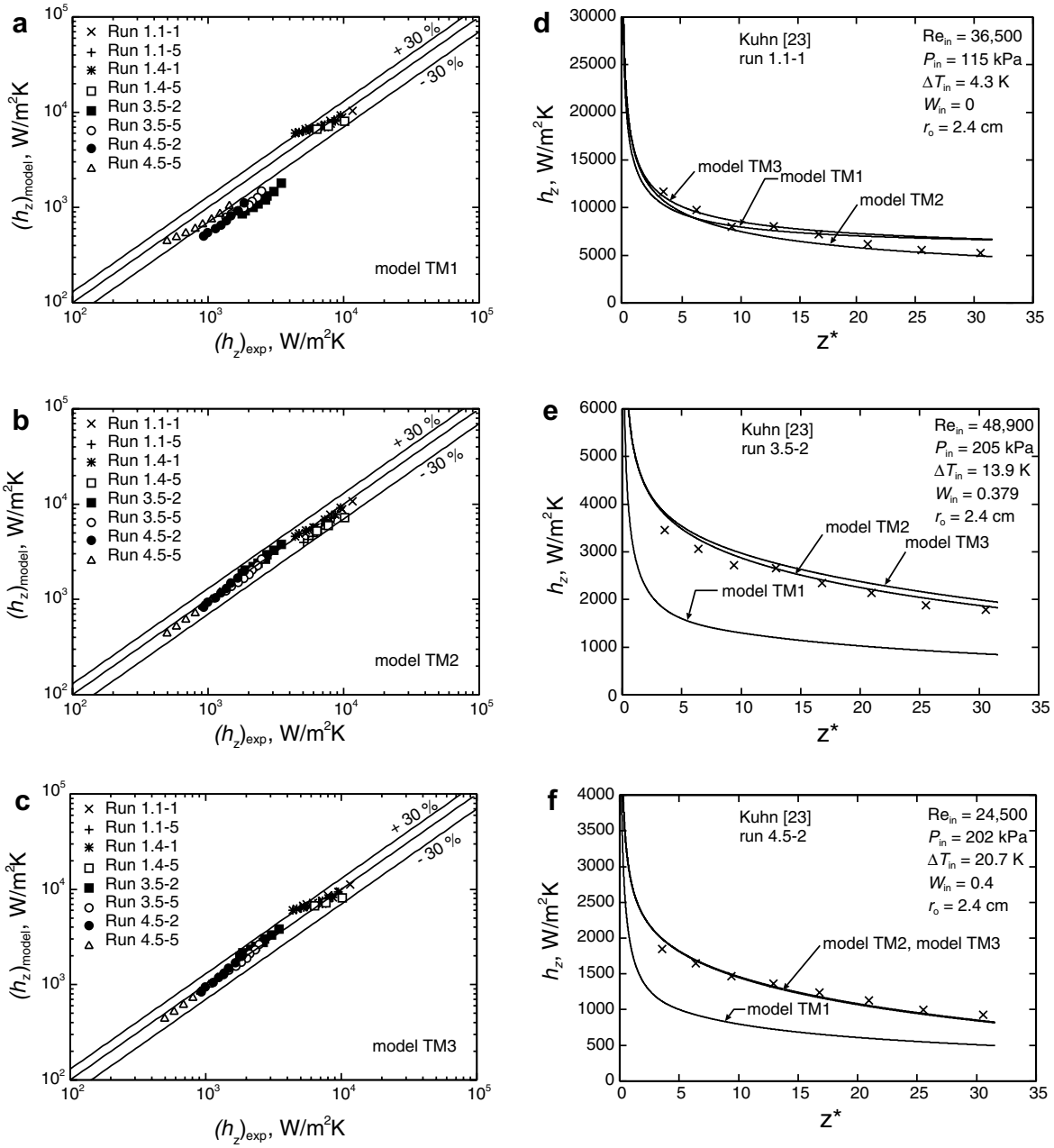

Fig. 6. Comparison with Kuhn [23] of overall heat transfer coefficient for eight runs using (a) model TM1, (b) model TM2, and (c) model TM3, and of local heat transfer coefficient using all three models for (a) run 1.1–1, (b) run 3.5–2, and (c) run 4.5–2.

isons, as this can have a large influence on the value of the local heat transfer coefficient. In all three experiments, the local heat transfer coefficient was calculated using

$$h_z = \frac{q''_z}{T_{sb} - T_{wall}} \tag{41}$$

where T_{sb} is the saturation temperature corresponding to the partial pressure of steam, evaluated at the average gas mass fraction across the tube. The wall heat flux is determined from an energy balance on the coolant in the annulus around the tube:

$$q''_z = \frac{-\dot{m}_{cw} C_{p,cw}}{\pi r_0} \frac{dT_{b,cw}}{dz} \tag{42}$$

where $T_{b,cw}$ is the local bulk temperature of the coolant. Goodykoontz and Dorsch [21], Siddique [22], and Kuhn [23] all used different methods to measure the coolant bulk temperature. Goodykoontz and Dorsch used one thermocouple in the annulus per axial measurement station and used that local temperature measurement as the coolant bulk temperature. Large errors could occur with this method for cases of low coolant Reynolds number, where large temperature differences across the annulus channel could exist. Siddique also used one thermocouple in the annulus at each axial measurement station. Mixing was promoted, however, by injecting air bubbles into the coolant flow. This method is designed to overcome the aforementioned drawback of the method used by Goodykoontz and Dorsch, but uncertainties due to local fluctuations still exist. Kuhn developed a new method of determining the coolant bulk temperature, based on measuring the annulus inner and outer wall temperatures. Kuhn numerically solved for the velocity and temperature profiles for thermally and hydrodynamically fully developed flow in an annulus. For a specific coolant mass flow rate, coolant properties, and geometry, Kuhn tabulated $T_{b,cw}$ as a function of the inner and outer annulus wall temperatures, which were measured by one pair of thermocouples at each axial measurement station. While this method relies on the assumption of fully developed conditions at all stations in the annulus, it was judged to be the most accurate of the three approaches [25]. It is noteworthy that it is with the experiment of Kuhn that the present numerical model showed the best agreement. Moreover, considering the comparison with experiments of the results of the three turbulence models, model TM2 showed the best agreement overall.

5. Results and discussion

A study was performed to examine the effects of changes to selected input parameters to the present model for steam-air flow in a vertical tube. For this study, turbulence model TM2 was chosen, uniform inlet profiles and constant wall temperature were prescribed, an inlet pressure of 1 atm was used, and the radius of the tube was 1 cm. Under these conditions, the remaining model input parameters are the inlet values of: the Reynolds number, the air mass fraction, and the difference in temperature between the mixture and the tube wall. In this study, the Reynolds number varied from 20,000 to 60,000, the air mass fraction varied from 0.0 to 0.2, and temperature differences of 5 K and 10 K were used. Sample detailed results of the axial development of the flow are presented first, followed by the results of a parametric study.

Fig. 7 presents plots of the axial variation of selected solution variable profiles for the case of inlet Reynolds number of 40,000, inlet air mass fraction equal to 0.1, and inlet temperature difference equal to 5 K. In Fig. 7a the profiles of the dimensionless axial velocity show the square inlet profile shape at $z^* = 0.01$. There is a slight increase in the peak mixture velocity near the inlet (at $z^* = 10$), followed

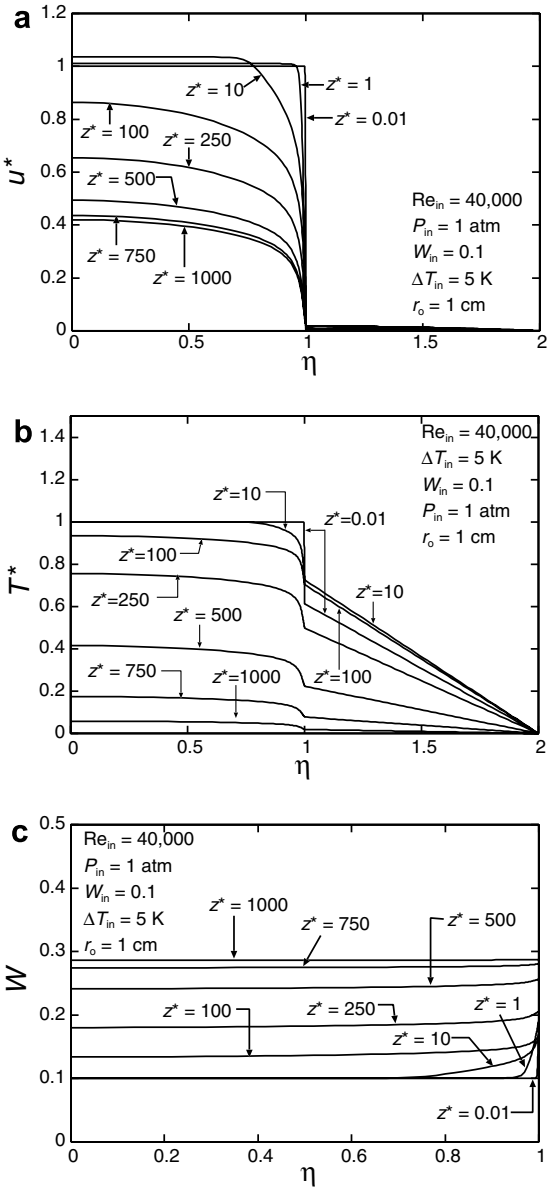

Fig. 7. Profiles of (a) dimensionless axial velocity, (b) dimensionless temperature, and (c) gas mass fraction at various axial locations for $Re_{in} = 40{,}000$, $P_{in} = 1$ atm, $W_{in} = 0.1$, $\Delta T_{in} = 5$ K, $r_0 = 1$ cm.

by a continuous reduction down the tube thereafter due to mass removal. The film velocity is increasing axially, and is much smaller in magnitude than that of the mixture. Fig. 7b illustrates how the dimensionless temperature is reduced by the axial build up of air. The temperature profiles also show a nearly linear shape in the film. In Fig. 7c, the aforementioned axial build up of air is clearly shown. In that graph it is also interesting to note the large gradient of W at the interface near the inlet (i.e., at $z^* < 10$) where the condensation rate is highest. The interface gradient of W is highest very near the inlet, and decreases axially. Examination of the film thickness showed rapid growth of the film near the inlet where the condensation rate is the greatest. As expected, the maximum Nusselt number occurs at the inlet, with a sharp decrease as the film builds up. Plots of the axial variation of the film thickness and local Nusselt number will be presented next with the discussion of the parametric study undertaken.

The effect on the model results of changing the inlet Reynolds number can be seen in Fig. 8. In Fig. 8a, the axial variation of film thickness shows predictions of decreased film thickness near the inlet as the Reynolds number is increased. Even though the condensation rate is higher for higher inlet Reynolds number, the film is initially thinner because the interface velocity is higher due to a significant influence of interfacial shear. Further along the tube, the interfacial shear becomes less significant and the film is thicker for higher inlet Reynolds number because of the increased inlet mass of vapor. The curves in Fig. 8b show that the local Nusselt number is initially greater for higher inlet Reynolds number and much smaller for all inlet Reynolds numbers at distances of z^* equal to 100 and greater. It is interesting to note, as shown in Fig. 8c, that the curves plotted in Fig. 8b nearly collapse onto one curve when local Nusselt number is normalized by the square root of the inlet Reynolds number.

Fig. 9 presents model results for two inlet temperature differences at two values of inlet Reynolds number. In Fig. 9a, the results show that, for a given inlet Reynolds number, the film thickness increased with increased ΔT_{in}. A greater temperature difference produces a greater condensation rate, which increases the film thickness. For

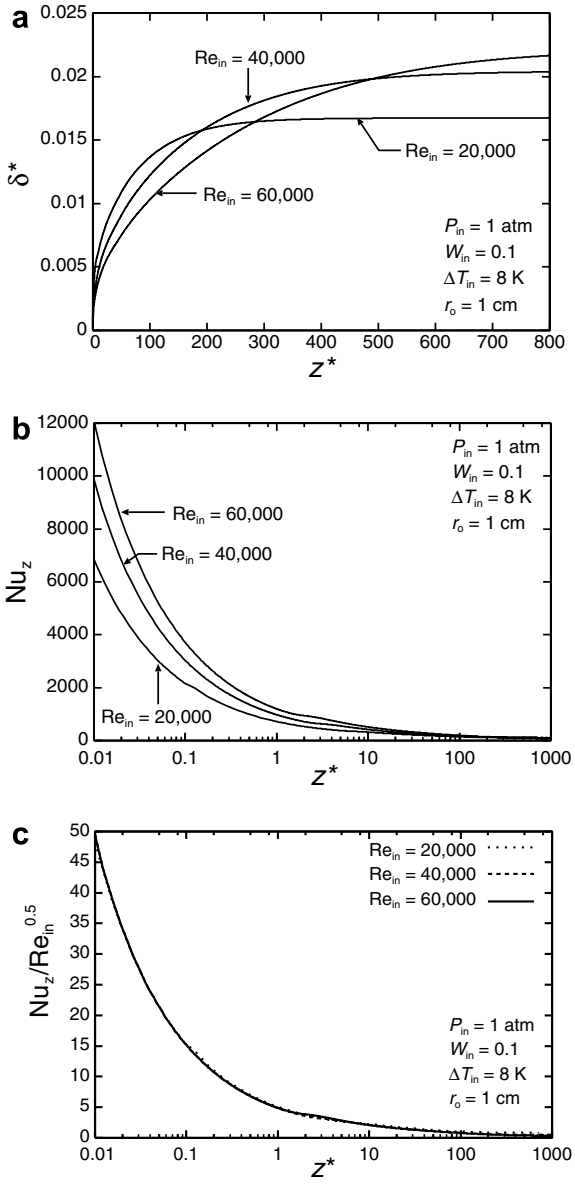

Fig. 8. Effect of change in Re_{in} on axial variation of (a) the dimensionless film thickness, (b) the local Nusselt number, and (c) $Nu_z/Re_{in}^{0.5}$ for $P_{in} = 1$ atm, $W_{in} = 0.1$, $\Delta T_{in} = 8$ K, $r_0 = 1$ cm.

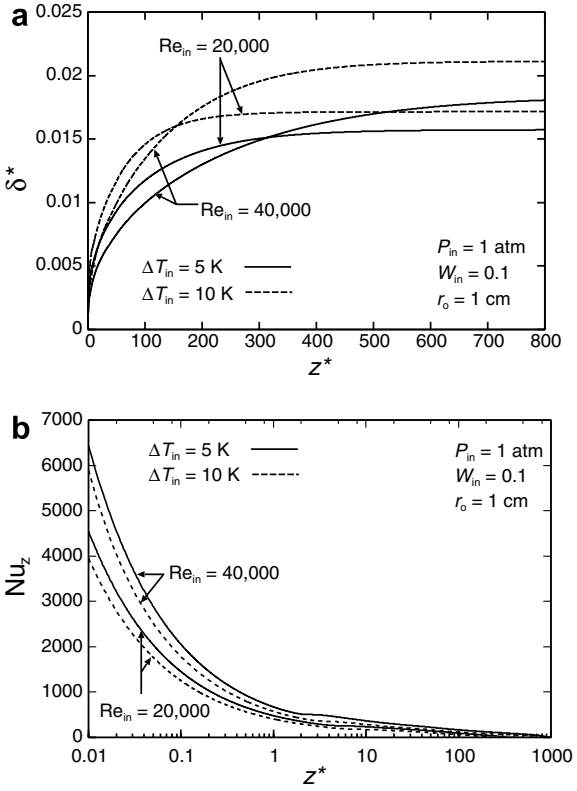

Fig. 9. Effect of change in ΔT_{in} on axial variation of (a) the dimensionless film thickness and (b) the local Nusselt number at two inlet Reynolds numbers for $P_{in} = 1$ atm, $W_{in} = 0.1$, $r_0 = 1$ cm.

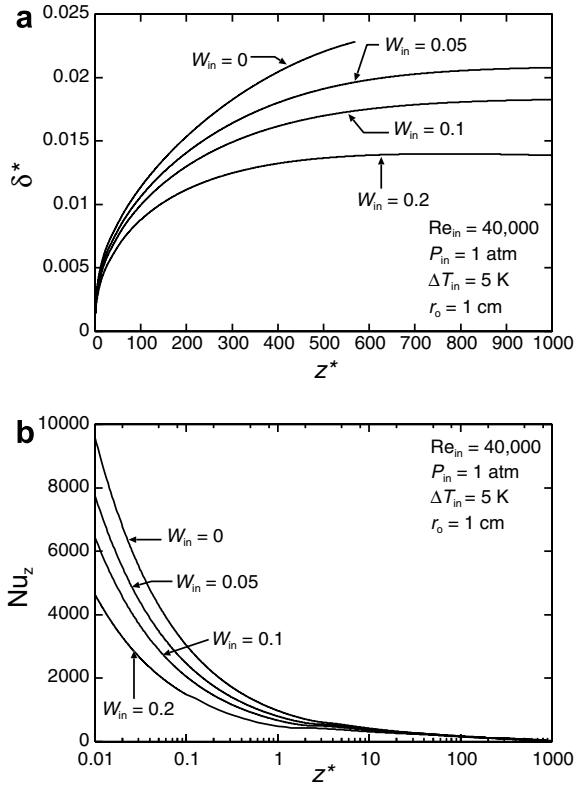

Fig. 10. Effect of change in W_{in} on axial variation of (a) the dimensionless film thickness and (b) the local Nusselt number for $Re_{in} = 40{,}000$, $P_{in} = 1$ atm, $\Delta T_{in} = 5$ K, $r_0 = 1$ cm.

a given ΔT_{in} , the effect of Reynolds number is the same as that seen in Fig. 8a: the film for the higher inlet Reynolds number is initially thinner, becoming thicker than the lower inlet Reynolds number film at some distance farther down the tube. Although it is not shown due to the scale used in Fig. 9a, it was noted that below $z^* = 25$, the film thicknesses for both temperature differences at Re_{in} of 40,000 were both thinner than the corresponding cases at Re_{in} of 20,000. Furthermore, for each Reynolds number, the higher temperature difference produced the thicker film. Farther down the tube, the $Re_{in} = 40{,}000$ cases of $\Delta T_{in} = 10$ K and $\Delta T_{in} = 5$ K developed to produce the thickest and second thickest films of the four cases, respectively. Fig. 9b shows that the local Nusselt number decreases with increased ΔT_{in}, even though the local heat flux increases with ΔT_{in}, due to the thicker film.

The effect on model predictions of changing the inlet air mass fraction is shown in Fig. 10. In Fig. 10a, the film thickness decreases with increased inlet air mass fraction due to the reduced condensation rate. For the case of pure steam under the conditions used, reverse flow was encountered at z^* of approximately 580. The reduction in condensation rate with increased gas mass fraction is also seen in Fig. 10b through the local Nusselt number reductions. For example, compared to the pure vapor case, the local Nusselt number at $z^* = 0.01$ is reduced by more than 30% for an inlet air mass fraction of just 10%.

6. Summary and conclusions

A numerical model is presented for film condensation from a turbulent gas–vapor mixture in axisymmetric downward flow in a vertical tube, based on the complete two-phase parabolic governing equations. No profile assumptions or additional correlation equations for interfacial heat and mass transfer are needed. Likewise, there was no use of a heat and mass transfer analogy, a diffusion layer, or a stagnant film analysis. A finite volume method was used for discretization of the governing equations of conservation of mass, momentum and energy in each of the liquid film and the mixture regions. A marching, fully coupled solution scheme is used on a mesh that adapts to the changing film thickness, which is a solution variable. Three turbulence models were used that are based on certain combinations of either a mixing length or a k–ε turbulence model in each of the two phases. The axial velocity, transverse-direction mass flux, temperature, gas mass fraction, film thickness, and local axial pressure gradient were computed using a fully coupled approach, with the turbulence model equations solved separately. This numerical model was compared with a total of 22 runs taken from three experiments for condensation of pure steam and from steam-air mixtures in vertical tubes. These comparisons covered a wide range of conditions and indicated that the turbulence model with the k–ε model in both phases produced the best overall predictions of the experiments. Other comparisons were made between the present model predictions and the results of two other numerical models and a correlation equation. In addition, a parametric study was performed on the effect of changing the inlet Reynolds number, the inlet-to-wall temperature difference, and the inlet gas mass fraction for steam-air mixtures. An increase in the inlet Reynolds number produced a film that is thinner near the inlet due to significant interfacial shear effects, but thicker overall further down the tube. An increase in the inlet-to-wall temperature difference produced thicker films due to a higher rate of condensation. Finally, an increase in the inlet gas mass fraction produced a thinner film due to the build up of gas at the liquid-mixture interface and a resultant reduction in the rate of condensation.

Acknowledgement

The financial assistance provided by the Natural Sciences and Engineering Research Council of Canada (NSERC), is gratefully acknowledged.

References

[1] W. Nusselt, Die oberflachenkondensation des wasserdampfes, Z. Ver. Deut. Ing. 60 (1916) 541–546.
[2] M.M. Shah, A general correlation for heat transfer during film condensation inside pipes, Int. J. Heat Mass Transfer 22 (1979) 547–556.
[3] S.L. Chen, F.M. Gerner, C.L. Tien, General film condensation correlations, Exp. Heat Transfer 1 (1987) 93–107.

[4] F. Dobran, R.S. Thorsen, Forced flow laminar filmwise condensation of a pure saturated vapor in a vertical tube, Int. J. Heat Mass Transfer 23 (1980) 161–177.
[5] J.A. Pohner, P.V. Desai, A two-fluid analysis of filmwise condensation in tubes, Int. J. Eng. Sci. 27 (5) (1989) 549–564.
[6] S.L. Chen, M.T. Ke, Forced convective film condensation inside vertical tubes, Int. J. Multiphase Flow 19 (6) (1993) 1045–1060.
[7] S.J. Kim, H.C. No, Turbulent film condensation of high pressure steam in a vertical tube, Int. J. Heat Mass Transfer 43 (2000) 4031–4042.
[8] S. Oh, S.T. Revankar, Analysis of the complete condensation in a vertical tube passive condenser, Int. Commun. Heat Mass Transfer 32 (2005) 716–727.
[9] R. Bellinghausen, U. Renz, Heat transfer and film thickness during condensation of steam flowing at high velocity in a vertical pipe, Int. J. Heat Mass Transfer 35 (3) (1992) 683–689.
[10] P.K. Panday, Two-dimensional turbulent film condensation of vapours flowing inside a vertical tube and between parallel plates: a numerical approach, Int. J. Refrig. 26 (2003) 492–503.
[11] R.H. Pletcher, Prediction of transpired turbulent boundary layers, Trans. ASME Heat Transfer 96C (1974) 89–94.
[12] C.Y. Wang, C.J. Tu, Effects of non-condensable gas on laminar film condensation in a vertical tube, Int. J. Heat Mass Transfer 31 (11) (1988) 2339–2345.
[13] M. Siddique, M.W. Golay, M.S. Kazimi, Theoretical modelling of forced convection condensation of steam in a vertical tube in the presence of a non-condensable gas, Nucl. Technol. 106 (1994) 202–215.
[14] A. Dehbi, S. Guentay, A model for the performance of a vertical tube condenser in the presence of noncondensable gases, Nucl. Energy Des. 177 (1997) 41–52.
[15] H.C. No, S.H. Park, Non-iterative condensation modeling for steam condensation with non-condensable gas in a vertical tube, Int. J. Heat Mass Transfer 45 (2002) 845–854.
[16] S.M. Ghiaasiaan, B.K. Kamboj, S.I. Abdel-Khalik, Two-fluid modeling of condensation in the presence of noncondensables in two-phase channel flows, Nucl. Sci. Eng. 119 (1995) 1–17.
[17] H.A. Hasanein, M.S. Kazimi, M.W. Golay, Forced convection in-tube steam condensation in the presence of noncondensable gases, Int. J. Heat Mass Transfer 39 (13) (1996) 2625–2639.
[18] S.T. Revankar, D. Pollock, Laminar film condensation in a vertical tube in the presence of noncondensable gas, Appl. Math. Modell. 29 (4) (2005) 341–359.
[19] R.Y. Yuann, Condensation from vapor–gas mixtures for forced downflow inside a tube, PhD thesis, University of California, Berkeley, CA, 1993.
[20] W.P. Jones, B.E. Launder, The predictions of laminarization with a two-equation model of turbulence, Int. J. Heat Mass Transfer 15 (1972) 301–314.
[21] J.H. Goodykoontz, R.G. Dorsch, Local heat transfer coefficients for condensation of steam in vertical downflow within a 5/8-inch-diameter tube, NASA Technical Note D-3326, NASA Lewis Research Center, Cleveland, Ohio, March 1966.
[22] M. Siddique, The effects of noncondensable gases on steam condensation under forced convection conditions, PhD thesis, Massachusetts Institute of Technology, Cambridge, MA, 1992.
[23] S.Z. Kuhn, Investigation of heat transfer from condensing steam-gas mixtures and turbulent film flowing downward inside a vertical tube, PhD thesis, University of California, Berkeley, CA, 1995.
[24] E.C. Siow, Numerical solution of two-phase model for laminar film condensation of vapour-gas mixtures in channels, M.Sc. thesis, University of Manitoba, Winnipeg, Manitoba, 2001.
[25] M.K. Groff, Numerical solution for turbulent film condensation from vapor–gas mixtures in vertical tubes, M.Sc. thesis, University of Manitoba, Winnipeg, Manitoba, 2005.
[26] J. Nikuradse, Gesetzmassigkeit der turbulenten stromung in glatten rohren, Ver. Deut. Ing. Forschung. 356 (1932).